https://doi.org/10.1016/j.apenergy.2023.121886

Revealing Interactions between the Operating Parameters of Protonic Ceramic Electrolysis Cell: A Modelling Study

Zheng Li[a], Idris Temitope Bello[a], Chen Wang[a], Na Yu[a], Xi Chen[a], Keqing Zheng[a,b]*, Meng Ni[a]*

a. Department of Building and Real Estate, Research Institute for Sustainable Urban Development (RISUD) & Research Institute for Smart Energy (RISE), The Hong Kong Polytechnic University, Hung Hom, Kowloon, Hong Kong, China
b. School of Low-Carbon Energy and Power Engineering, China University of Mining and Technology, Xuzhou, 221116, Jiangsu, China

* Corresponding authors
Email: meng.ni@polyu.edu.hk (M. Ni)
keqingzheng@cumt.edu.cn (K. Zheng)

Abstract

Protonic ceramic electrolysis cell (PCEC) is a clean and sustainable technology for hydrogen production. To provide a comprehensive understanding of the effects of various parameters on the performance of PCEC, a framework is proposed to combine the 2D numerical model with One-Factor-At-a-Time (OFAT) and Design of Experiments (DOE) methods. DOE is a simple but effective method to gain deep insight into the effect of different factors on the response variable using a small number of cases. In the OFAT result, a peak optimal Faradaic efficiency (FE) of 82% is found at 600°C and a current density of 0.4 A cm^{-2}. The FE increases with the increasing inlet flow rate, while the temperature gradient reduces continuously. It is also found that if the inlet steam mole fraction increases by 5%, the FE can be increased by at least 0.25%. DOE results demonstrate the most important factors are the anodic inlet steam molar fraction and anodic inlet flow rate. Additionally, the interaction effects between them are also found to be significant. Noteworthy, regression models derived from DOE results also demonstrate potential capabilities as surrogate models for 2D numerical model. Therefore, DOE is a powerful tool that can draw rigorous conclusions while saving a lot of computational resources. Overall, this study provides deep insights into the interaction effects of different parameters. The framework proposed in this study can be applied to guide future PCEC design optimization.

Keywords

Protonic ceramic electrolysis cell; Numerical modelling; Design of Experiments; One-Factor-At-a-Time.

Nomenclature

Abbreviation

PCFC	Protonic ceramic fuel cell
AEC	Alkaline electrolysis cell
PEMEC	Proton exchange membrane electrolysis cell
SOEC	Solid oxide electrolysis cell
FE	Faradaic efficiency
NPP	Nernst-Planck-Poisson
TPB	Triple phase boundary
TNV	Thermal-neutral voltage

Letter

k_i	Reaction rate coefficient
A_i	Pre-exponential factor
T	Absolute temperature, K
n	Temperature exponent
E_{act}	Activation energy, J mol^{-1}
R	Universal molar gas constant, 8.314 J mol^{-1} k^{-1}
E_{eq}	Equilibrium potential, V
c_i	Concentration, mol m^{-3}
J_i	Molar flux, mol m^{-2} s^{-1}
F	Faraday constant, 96485.3 C mol^{-1}
z_i	Number of charges
ϕ_{el}	Electrostatic potential, V
i	Current density, A m^{-2}
y_i	Molar fraction of species i, mol s^{-1}
V_m	Molar volume, m^{-3} mol
K_{eq}	Reaction rate equilibrium constant
ΔH^0	Change of enthalpy, J mol^{-1}
ΔS^0	Change of entropy, J mol^{-1} K^{-1}

v_s	Volume fraction
P_{per}	Percolation probability
λ_{TPB}^{eff}	Effective TPB, $m^2\ m^{-3}$
M_i	Molar mass of species i, $kg\ mol^{-1}$
$\boldsymbol{u}$	Velocity, $m\ s^{-1}$
$\boldsymbol{N}_i$	Molar flux of species I, $mol\ m^{-2}\ s^{-1}$
D_{iK}^{eff}	Effective Knudsen diffusion coefficient of species i, $m^2\ s^{-1}$
D_{ij}^{eff}	Effective binary diffusion coefficient, $m^2\ s^{-1}$
C_p	Thermal capacity, $J\ mol^{-1}\ k^{-1}$
λ_{eff}	Effective thermal conductivity, $W\ m^{-1}\ k^{-1}$
Q_i	Source term i
$x_{an/ca,inlet}$	Inlet composition at the anode/cathode side gas channel, %
$v_{an/ca,inlet}$	Inlet volumetric flow rate at the anode/cathode side gas channel
ρ	Density, $kg\ m^{-3}$
σ	Conductivity, $S\ m^{-1}$
ε	Porosity
τ	Tortuosity
k	Permeability, m^2
ω_i	Mass fraction of species i
μ	Viscosity, Pa s

1. Introduction

Currently, the world is facing an energy crisis, with fossil fuels being over-utilized and causing damage to the environment. Alternative and clean fuels are required to meet the growing demands and to reduce the carbon emission. Hydrogen, a clean and renewable energy carrier, is likely to play an essential role in the future zero-carbon society [1]. Hydrogen element is abundant on Earth from a variety of sources, including natural gas, water, and biomass, but hydrogen gas is not readily available. To date, the dominant method to produce hydrogen is still hydrocarbon reforming, which is an energy-intensive process [2]. For example, nearly 95% hydrogen production in the U.S. comes from natural gas reforming, which is carbon-expensive [3]. In order to minimize the carbon footprint of the hydrogen production process, developing clean and efficient hydrogen-producing technology is becoming increasingly important [4].

Compared with solar photocatalysis water splitting and solar thermochemical cycle water splitting technologies, water electrolysis cells driven by solar power has great potential for large scale clean hydrogen production due to their high efficiency and durable operation. Room temperature alkaline electrolysis cell (AEC) and proton exchange membrane electrolysis cell (PEMEC) require high voltage thus high power consumption for hydrogen production. High temperature solid oxide electrolysis cell (SOEC) shows much lower voltage (low power consumption) and high current density thus high hydrogen production rate. However, the too high operating temperature (about 800 °C) of SOEC requires complicated thermal management causes high system cost and poor SOEC durability especially under fluctuating operation conditions. For comparison, protonic ceramic electrolysis cell (PCEC) can work at about 400 °C – 600 °C, which simplifies the thermal management system, reduces the system cost and improves the cell durability. Furthermore, since the activation energy of protons is smaller than that of oxygen ions, the conductivity of a typical proton conductor (BCZY, 1.49 S m^{-1}) is greater than that of a typical oxygen ion conductor (YSZ, 0.25 S m^{-1}) at 600 °C [5,6]. This

indicates that PCEC may achieve a lower ohmic overpotential, resulting in a lower power consumption. Therefore, PCEC is more promising than SOEC at intermediate temperatures. Compared with various electrolysis technologies, PCEC is an attractive option for powering the future hydrogen society.

The theoretical model of PCEC dates to 2008. Ni et al. develop a 1D model of PCEC [7]. They compared the performance of PCEC and solid oxide electrolysis cell (SOEC). It was found that PCEC is advantageous over SOEC in terms of structural design. However, in their model, the electrolyte is considered to be a pure proton conductor, without considering the current leakage and possible oxygen ion conduction. The current leakage phenomenon is experimentally observed in the protonic ceramic electrolyte [8]. This implies that not all the current supplied to the PCEC can be converted to hydrogen. In other words, it is difficult for PCEC to achieve 100% Faradaic efficiency (FE). This is also a major challenge for the development of PCEC. For example, in Ref [9], Choi et al. developed a highly active air electrode $PrBa_{0.5}Sr_{0.5}Co_{1.5}Fe_{0.5}O_{5+\delta}$ (PBSCF) for their PCEC. They reported a measured FE of 76% at 600 °C, 1.3 V for their PCEC. Consequently, the current leakage can significantly affect the performance of PCEC. Including the current leakage phenomenon in the numerical model is of great importance to understanding the operating mechanism of PCEC. Zhang and co-workers developed a numerical model to account for the current leakage in the yttria-doped barium zirconate ($BaZr_{0.8}Y_{0.2}O_3$, BZY20), which is a widely-used proton-conducting electrolyte material for PCEC [10]. Notably, an analytical solution was derived in their work to describe the leakage currents in the proton-ceramic electrolyte. They also found that the FE at a high temperature is generally lower than that at a low temperature. Kee et al. developed a numerical model to investigate the defect transport in the radial direction through the BZY20 [11]. Both steady-state and transient behaviours of the BZY20 membrane are simulated. Unlike Zhang, who used the analytical equation to describe the leakage current in the BZY20 membrane, Kee

and co-workers developed a Nernst-Planck-Poisson (NPP) model to describe the transport of different charge carriers through the BZY20 membrane. As a result, this NPP model can systematically describe the complex transport process through the electrolyte, thereby unveiling the mechanism of leakage currents. Thereafter, Zhu et al further applied this NPP model to the PCEC, in which BZY10 was used as the electrolyte material [12]. The effects of environmental atmosphere composition on the open circuit voltage of PCEC are well-investigated in their work. Their 1D model results showed that the FE increased with decreasing operating temperature and increasing voltage. Although the previous studies could describe the complicated transport process within the electrolyte, they did not consider heat transport within the PCEC. The heat transport can significantly affect the temperature distribution in the PCEC, thereby affecting the performance of the PCEC. In addition, as previous studies reveal, the FE of PCEC is sensitive to temperature. Hence, taking heat transport into account can provide a better understanding of the current leakage phenomenon in PCEC.

Aiming to fill this research gap, the present study develops a 2D numerical model, in which the heat transport and charge transport within the PCEC are fully considered. More importantly, to explore the effects of different operating parameters on the PCEC performance, two methods are applied in this study: 1) One-Factor-At-a-Time (OFAT) method; 2) Design of Experiments (DOE). The OFAT method, where one factor or parameter is varied at a time while keeping all other factors constant, aims to study the effect of each factor on the outcome variable independently of other factors [13]. Although the OFAT method is easy to implement and can help researchers to understand the effect of a factor, it cannot account for interactions between different factors, which may pose a significant impact on the outcome as many parameters of PCEC may interact with each other. The second method, DOE, can well address the limitations by fully consider the interactions between parameters [14]. It is thus expected that the DOE

method can not only provide insights on the influences of parameters on PCEC performance, but also enable multi-parameter optimization to achieve the best performance of PCEC. The framework of this study is shown in Figure 1. The present work combines the advantages of OFAT and DOE methods, thereby providing a more accurate understanding of the effects of different parameters on the PCEC. Furthermore, the framework proposed in this study can be extended to other theoretical modelling of PCEC.

2. Modelling methods

2.1 Modelling geometry

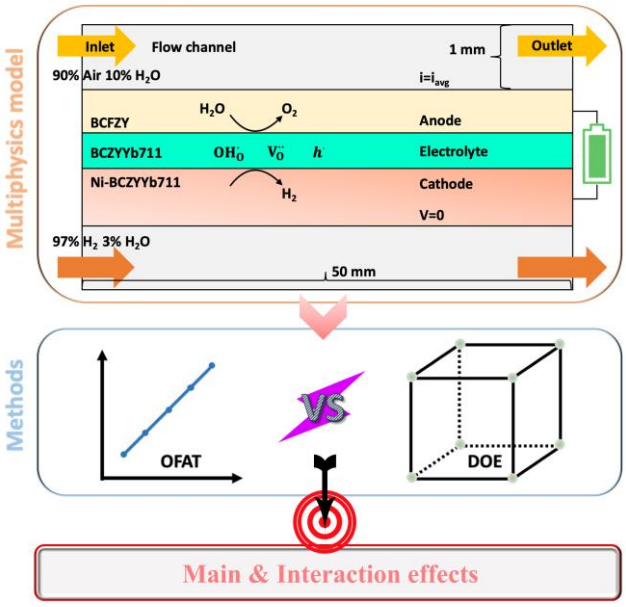

Figure 1 Schematic of the framework to reveal the main and interaction effects.

Figure 1 shows the framework of this study. Firstly, the 2D Multiphysics model is developed. Secondly, the OFAT and DOE methods are respectively utilized to create a sequence of inputs for the 2D Multiphysics model. Thirdly, the OFAT approach can provide insight into the individual effects of each parameter on the behaviour of PCEC, while the DOE method can reveal the individual effects and interactions between different parameters on PCEC behaviour, as opposed to analysing them in isolation. Therefore, the OFAT and DOE methods are compared to fully demonstrate the impact of various parameters on the performance of PCEC.

Additionally, this comparison can help to uncover the characteristics of each method during the analysis process. A 2D Multiphysics model is developed for a planar PCEC (active area: 5 × 5 cm^2). The PCEC length is along the horizontal direction, while the PCEC thickness is along the vertical direction. After the construction of the model, both OFAT and DOE approaches are implemented to investigate the effects of different operating parameters. The model parameters and geometry information are gathered in Table 1. The main assumptions applied in this 2D model are shown below:

1) All the gas species (H_2, H_2O, O_2, N_2) are considered ideal and incompressible gases.
2) Both electrolyte and electrode particles are uniformly distributed within the porous electrodes.
3) PCEC is assumed to be operated under steady state operation.
4) The electrochemical reaction sites are uniformly distributed within the porous electrodes.
5) The protonic defects, oxygen vacancies and electronic holes are considered mobile charge carriers in the electrolyte material.

Table 1 2D model parameters.

Parameters/Locations	**Value/expression**	**Unit**
Anode thickness	30	μm
Cathode thickness	400	μm
Electrolyte thickness	20	μm
Gas channel thickness	1	mm
Out-of-Plane thickness	50	mm
Cell length	50	mm
ε_{an}	0.4	1
ε_{ca}	0.4	1
$\tau_{an/ca}$	3	1
P_{op}	1	atm

T_{op}	823.15	K
$r_{particle}$	0.5	μm
$V_{s,\,an}$	0.6	1
$V_{s,ca}$	0.6	1

2.2 Electrochemical model

In the PCEC, the two half-electrochemical reactions in the anode and cathode can be written in the reduction reaction form as:

$$Anode: O_2(g) + 4[OH_O^{\cdot}] + 4e^- \leftrightharpoons 2H_2O(g) + 4[O_O^{\times}] \quad (1)$$

$$Cathode: 2OH_O^{\cdot} + 2e' \leftrightharpoons H_2(g) + 2O_O^{\times} \quad (2)$$

The Butler-Volmer equation is applied to describe the charge-transfer reaction rate in the anode and cathode, respectively [15].

$$i_a = i_{0,a}[\exp\left(\frac{\alpha_a F\eta_{act,a}}{RT}\right) - \exp\left(\frac{-(1-\alpha_a)F\eta_{act,a}}{RT}\right)] \quad (3)$$

$$i_c = i_{0,c}[\exp\left(\frac{\alpha_c F\eta_{act,c}}{RT}\right) - \exp\left(\frac{-(1-\alpha_c)F\eta_{act,c}}{RT}\right)] \quad (4)$$

Where $\alpha_{a/c}$ is the anodic/cathodic charge transfer number, $\eta_{act,a/c}$ represents the anodic/cathodic activation overpotential (V), $i_{0,a/c}$ represents the anodic/cathodic exchange current density (A m^{-2}) [16], which can be given by:

$$i_{0,a} = \gamma_{0,a}\exp\left(-\frac{E_{act,a}}{RT}\right)[OH_O^{\cdot}]^{\beta_a}[O_O^{\times}]^{1-\beta_a}p_{O_2}^{0.25}p_{H_2O} \quad (5)$$

$$i_{0,c} = \gamma_{0,c}\exp\left(-\frac{E_{act,c}}{RT}\right)[OH_O^{\cdot}]^{\beta_c}[O_O^{\times}]^{1-\beta_c}p_{H_2} \quad (6)$$

Where $y_{0,a/c}$ is anodic/cathodic pre-exponential factor of exchange current density, $E_{act,a/c}$ is the anodic/cathodic activation energy (J mol^{-1}), p_i is the partial gas pressure of gas species i. The source term of current in the porous electrode is calculated as:

$$S_i = \lambda_{TPB}^{eff} \cdot i \quad (7)$$

Where λ_{TPB}^{eff} is the effective triple phase boundaries (TPB) length per unit volume (m^2 m^{-3}). λ_{TPB}^{eff} in the porous electrode can be calculated as [17]:

$$\lambda_{TPB}^{eff} = 2\pi \min(r_{ed}, r_{el})^2 P_{per,ed} P_{per,el} \sin\left(\frac{\theta}{2}\right) n_{ed}^{v} \quad (8)$$

$$n_{ed}^{v} = \frac{(1-\varepsilon) v_s}{\frac{4}{3}\pi r_{ed}^3} \quad (9)$$

$$P_{per} = 1 - \left[\left(\frac{4.236 - Z_{k,k}}{2.472}\right)^{2.5}\right]^{0.4} \quad (10)$$

Where $r_{ed/el}$ represents the radius of the electrode/electrolyte particles (m), θ is the contact angle (15°), n_{ed}^{v} is the number density of electrode particles (m^{-3}), ε is the porosity, v_s is the volume fraction, P_{per} is the percolation probability of electrode or electrolyte materials, $Z_{k,k}$ is the average contact number between k particles [18].

2.3 Charge transfer

The charge transfer process within the electrolyte is described by the Nernst-Planck equation, where both diffusion and migration of charge carriers within the electrolyte material are taken into account [19]:

$$J_i = -D_i^{eff} \left(\nabla c_i + \frac{z_i F}{RT} c_i \nabla \phi_{el}\right) \quad (11)$$

Where J_i is the molar flux of species i (mol m^{-2} s^{-1}), D_i^{eff} represents the effective diffusion coefficient (m^2 s^{-1}), F is the Faraday constant (96458.3 C mol^{-1}), c_i is the concentration of species i (mol m^{-3}). The conservation equation of mobile charge carriers within the electrolyte can be given by:

$$\frac{\partial c_i}{\partial t} + \nabla \cdot J_i = s_d \quad (12)$$

Where s_d is the source term describing the defect species' production or consumption owing to the defect chemical reactions. The last term in Eq.11, ϕ_{el}, is the electrostatic potential. Poisson equation portrays the relationship between electrostatic potential and local charge density as [20]:

$$\nabla \cdot (\varepsilon_{abs} \nabla \phi_{el}) + F \sum_i z_i c_i = 0 \tag{13}$$

Where ε_{abs} stands for the absolute permittivity (F m^{-1}) of the electrolyte, z_i is the number of charges carried by species i. The current density of a species i (i_i) or the overall external current density (i_{ex}) both can be derived through the molar flux calculated from Eq.11.

$$i_i = z_i F J_i \tag{14}$$

$$i_{ex} = F \sum_i z_i J_i = \sum_i i_i \tag{15}$$

Besides, to solve the above Nernst-Planck-Poisson equations, the concentrations of different defect species are essential as the boundary conditions. Three defect chemical reactions, involving four defect species ($O_O^\times$, $OH_O^\cdot$, $V_O^{\cdot\cdot}$, $O_O^\cdot$) and three gas species (H_2, H_2O, O_2), are taken into consideration under wet condition [19]:

$$0.5H_2 + O_O^\cdot \leftrightharpoons OH_O^\cdot \tag{16}$$

$$H_2O + O_O^\times + V_O^{\cdot\cdot} \leftrightharpoons 2OH_O^\cdot \tag{17}$$

$$0.5O_2 + O_O^\times + V_O^{\cdot\cdot} \leftrightharpoons 2O_O^\cdot \tag{18}$$

Where $O_O^\times$, $OH_O^\cdot$, $V_O^{\cdot\cdot}$, $O_O^\cdot$ stand for the lattice oxygen site, protonic defect, oxygen vacancy and oxygen-site polaron, respectively. Therefore, the reaction rates of the three reactions (Eqs. 16-18) can be expressed by:

$$r_1 = k_{f1} c_{H_2}^{0.5} c_{O_O^\cdot} - k_{b1} c_{OH_O^\cdot} \tag{19}$$

$$r_2 = k_{f2} c_{H_2O} c_{O_O^\times} c_{V_O^{\cdot\cdot}} - k_{b2} c_{OH_O^\cdot}^2 \tag{20}$$

$$r_3 = k_{f3} c_{O_2}^{0.5} c_{O_O^\times} c_{V_O^{\cdot\cdot}} - k_{b2} c_{O_O^{\cdot}}^2 \tag{21}$$

Where k_f and k_b are the forward and backward reaction rate constants, respectively. The ratio of k_f to k_b equals to the equilibrium constant for each reaction. Moreover, the equilibrium of the three reactions can be calculated as [21]:

$$K_{p,H_2} = \frac{[OH_O^{\cdot}]}{[O_O^{\cdot}] p_{H_2}^{0.5}} \tag{22}$$

$$K_{p,H_2O} = \frac{[OH_O^{\cdot}]^2}{[O_O^\times][V_O^{\cdot\cdot}] p_{H_2O}} \tag{23}$$

$$K_{p,O_2} = \frac{[O_O^{\cdot}]^2}{[O_O^\times][V_O^{\cdot\cdot}] p_{O_2}^{0.5}} \tag{24}$$

where [i] is the molar concentration (mol m^{-3}) of defect species i. The defect unit concentration ($[i]_L$) can be derived from the molar concentration:

$$[X_B]_L = [X_B] V_m \tag{25}$$

where V_m is the molar volume (m^3 mol^{-1}). In addition, through the entropy change (ΔS°) and enthalpy change (ΔH°), the equilibrium constant can be defined as:

$$K = \exp\left(\frac{\Delta S^\circ}{R}\right) \cdot \exp\left(-\frac{\Delta H^\circ}{RT}\right) \tag{26}$$

Noteworthy, the parameters of the different defect reactions can be found in Ref. [19]. Furthermore, to solve the defect concentrations within the electrolyte, two additional constraints are required. The first is the electroneutrality, the second is the O-site conservation condition.

$$[OH_O^{\cdot}] + 2[V_O^{\cdot\cdot}] + [O_O^{\cdot}] - [Yb_{Zr}'] = 0 \tag{27}$$

$$[OH_O^{\cdot}] + [V_O^{\cdot\cdot}] + [O_O^{\cdot}] + [O_O^\times] = 3 \tag{28}$$

The conductivity of a charge carrier i in the electrolyte can be calculated once the defect concentration is obtained.

$$\sigma_i = \frac{F^2}{RT} z_i^2 c_i D_i \tag{29}$$

$$D_i = D^0 \exp\left(-\frac{E_{act,d}}{RT}\right) \tag{30}$$

where D^0 is the pre-exponential constant, $E_{act,d}$ represents the activation energy (unit), both of which can be found in Ref. [22]. The sum of the conductivities of different charge carriers is the total conductivity of the electrolyte.

$$\sigma_{el} = \sum_i \frac{F^2}{RT} z_i^2 c_i D_i \tag{31}$$

In addition to the charge transfer within the electrolyte, the electrons transfer within the electrode can be described by Ohm's law [23]:

$$\nabla \cdot \boldsymbol{i}_e = \nabla \cdot (\sigma_{e,eff} \nabla \phi_e) \tag{32}$$

Where $\boldsymbol{i}_e$ is the electronic current vector, $\sigma_{e,eff}$ is the effective electronic conductivity (S m^{-1}), which can be determined as [24]:

$$\sigma_{eff} = \sigma_0 \left[(1-\varepsilon) v_s P_{per}\right]^{\zeta} \tag{33}$$

Where σ_0 and ζ are the intrinsic conductivity and Bruggeman factor, respectively.

2.4 Mass and momentum transport

The dusty gas model is implemented to describe the species transport in the PCEC, in which both molecular diffusion and Knudsen diffusion are taken into account [25]:

$$\frac{\boldsymbol{N}_i}{D_{iK}^{eff}} + \sum_{j=1}^{n} \frac{y_j \boldsymbol{N}_i - y_i \boldsymbol{N}_j}{D_{ij}^{eff}} = -\frac{1}{RT}\left(P\nabla y_i + y_i \nabla P + y_i \nabla P \frac{kP}{D_{iK}^{eff}\mu}\right) \tag{34}$$

$$D_{iK}^{eff} = \frac{\varepsilon}{\tau}\frac{2}{3} r_p \sqrt{\frac{8RT}{\pi M_i}} \tag{35}$$

$$r_p = \frac{2}{3}\frac{\varepsilon}{1-\varepsilon}\frac{1}{V_{s,ed}/r_{ed} + V_{s,el}/r_{el}} \tag{36}$$

$$D_{ij}^{eff} = \frac{\varepsilon}{\tau} \cdot D_{ij}^{0} \tag{37}$$

$$D_{ij}^{0} = \frac{0.042851 \times \left(\frac{1}{M_i} + \frac{1}{M_j}\right)^{-0.5} - 0.0098 \times T^{1.5}}{P\Omega_D \sigma_{ij}^2} \tag{38}$$

Where y_i is the mole fraction of gas species i, $\boldsymbol{N}_i$ is the molar flux of specie i (mol m^{-2} s^{-1}), D_{iK}^{eff} represents the effective Knudsen diffusion coefficient of species i (m^2 s^{-1}), D_{ij}^{eff} represents the effective binary diffusion coefficient (m^2 s^{-1}), τ stands for the tortuosity of porous electrode, r_p is the radius of pore, D_{ij}^{0} denotes the binary molecular diffusion coefficient (m^2 s^{-1}). This coefficient can be determined by a modified Chapman-Enskog relation [26–28].

In addition, the momentum transport in the porous media can be described by the Darcy's term modified Navier-Stokes equation [29,30]:

$$\frac{\rho}{\varepsilon}(\boldsymbol{u}\cdot\nabla)\cdot\frac{\boldsymbol{u}}{\varepsilon} = -\nabla P + \nabla\cdot\left[\frac{\mu}{\varepsilon}(\nabla\boldsymbol{u} + \nabla\boldsymbol{u}^T) - \frac{2}{3}\frac{\mu}{\varepsilon}(\nabla\cdot\boldsymbol{u})\right] - \left(\mu\kappa^{-1} + \frac{Q_m}{\varepsilon^2}\right)\boldsymbol{u} \tag{39}$$

$$\rho\nabla\cdot\boldsymbol{u} = Q_m = \sum y_i R_i \tag{40}$$

$$\rho = \frac{P}{RT}\sum_i \frac{\omega_i}{M_i} \tag{41}$$

Where ρ stands for the density (kg m^{-3}), $\boldsymbol{u}$ is the velocity vector (m s^{-1}), μ is the viscosity (Pa s^{-1}), κ signifies the permeability, Q_m is the source term of mass determined by the reaction rates.

2.5 Heat transfer

The heat transfer within the electrolysis cell is described by the following formula [31]:

$$\rho C_{p,eff}\boldsymbol{u}\nabla T + \nabla\cdot\left(-\lambda_{eff}\nabla T\right) = Q_h \tag{42}$$

Where C_p in the first term represents the effective specific heat capacity (J kg^{-1} K^{-1}), while λ_{eff} in the second term signifies the effective thermal conductivity (W m^{-1} K^{-1}). Q_h represents the

source term, including the electrochemical reaction heat, ohmic heat, and heat due to the polarization loss [32].

2.6 Boundary conditions

The boundary conditions applied for solving the 2D model are summarized in the Table 2. The model is solved by the finite element method in COMSOL Multiphysics. Mesh independence is obtained with 259338 DOF. The presented model is validated (Figure 2 (a)) against the experimental data of a button-cell operating under fuel cell mode [21].

Table 2 The boundary conditions of PCEC model.

Condition/Locations	Value	Unit
$x_{ca,inlet}$	Humidified air (10% H_2O)	
$x_{an,inlet}$	97% H_2/3% H_2O	
$v_{ca,inlet}$	1.03×10^{-6}	kg s^{-1}
$v_{an,inlet}$	1.03×10^{-4}	kg s^{-1}
i_{avg}	0.5	A m^{-2}
Anode inlet	$x_{an,inlet}, v_{an,inlet}, T_{op}$	
Cathode inlet	$x_{ca,inlet}, v_{ca,inlet}, T_{op}$	
Anode upper-face	$i = i_{avg}$	
Cathode upper-face	$\varphi_e = 0$	
Anode outlet	Open boundary	
Cathode outlet	Open boundary	
Other boundaries	Insulation/Wall	

3. Design of Experiments (DOE) Method

In this work, a design of experiments (DOE) method, combined with the 2D model, is implemented to perform a more systematic parametric analysis than the traditional OFAT method. Furthermore, DOE can effectively identify the most important parameters and reveal how different operating parameters interact with each other. DOE is a method that

systematically varies multiple factors between different levels (e.g., two levels in this case) to create combinations that can be tested and analyzed to determine the main and interactive effects on the response variables of interest. This method produces structured and statistically informed outcomes, unlike the OFAT approach, which could require many experiments to achieve the desired results. Therefore, DOE can provide insight into how different factors affect the response variables with a small number of cases. This is because DOE uses a structured experimental design that ensures that each factor is varied systematically across the different treatments, which allows researchers to isolate the effects of each individual factor. In particular, in this work, we apply a well-known Yates technique to perform a full 2^4 factorial design (16 cases) [1]. By using the factorial design, DOE can effectively control for the effects of irrelevant variables and isolate the effects of factors of interest. In addition to applying a systematic factorial design, DOE also employs analysis of variance (a statistical technique) to analyze the data collected. Then, it can quantify the impacts of different factors and identify the most important factor. Thus, by carefully conducting a factorial design in DOE and performing statistical analysis of the results, valuable insights can be gained even with a limited number of cases. To gain a better understanding and learn about the DOE method, Refs [34,35] are highly recommended as they are excellent textbooks on the subject. Furthermore, additional literature utilizing the DOE method can be found in Refs [36,37]. These resources provide valuable insights and guidance on how to effectively design experiments and analyse data using the DOE method. By utilizing these resources, researchers can gain a deeper understanding of the DOE method and apply it more effectively to the research.

Four factors are chosen: the cathodic inlet steam molar fraction (xc_in, denoted as A), the anodic inlet steam molar fraction (xa_in, denoted as B), the cathodic inlet flow rate (vc_in, denoted as C) and the anodic inlet flow rate (va_in, denoted as D). Two levels, i.e., high level (coded as 1) and low level (coded as 0), are assigned to each factor. Hence, the total 16

treatments are included. Three replications are performed to ensure the precision of the data. Additionally, three important responses are recorded, namely, applied voltage, temperature gradient and faraday efficiency. The 2^4 factorial design is shown in Table 3. The high-level and low-level values of different parameters are summarized in Table 4.

Table 3 The list of 2^4 factorial design.

ID	**A, xc_in**	**B, xa_in**	**C, vc_in**	**D, va_in**	**Treatment combination**
1	0	0	0	0	(1)
2	1	0	0	0	A
3	0	1	0	0	B
4	1	1	0	0	AB
5	0	0	1	0	C
6	1	0	1	0	AC
7	0	1	1	0	BC
8	1	1	1	0	ABC
9	0	0	0	1	D
10	1	0	0	1	AD
11	0	1	0	1	BD
12	1	1	0	1	ABD
13	0	0	1	1	CD
14	1	0	1	1	ACD
15	0	1	1	1	BCD
16	1	1	1	1	ABCD

Table 4 The high-level and low-level of four operating parameters.

Factors	**High-level**	**Low-level**
A, xc_in	0.05	0.45
B, xa_in	0.1	0.5
C, vc_in	8.38×10^{-7} kg s^{-1}	1.47×10^{-6} kg s^{-1}

D, va_in	6.19×10^{-5} kg s^{-1}	1.24×10^{-4} kg s^{-1}

4. Results and Discussion

4.1 OFAT

4.1.1 Effects of current density and working temperature

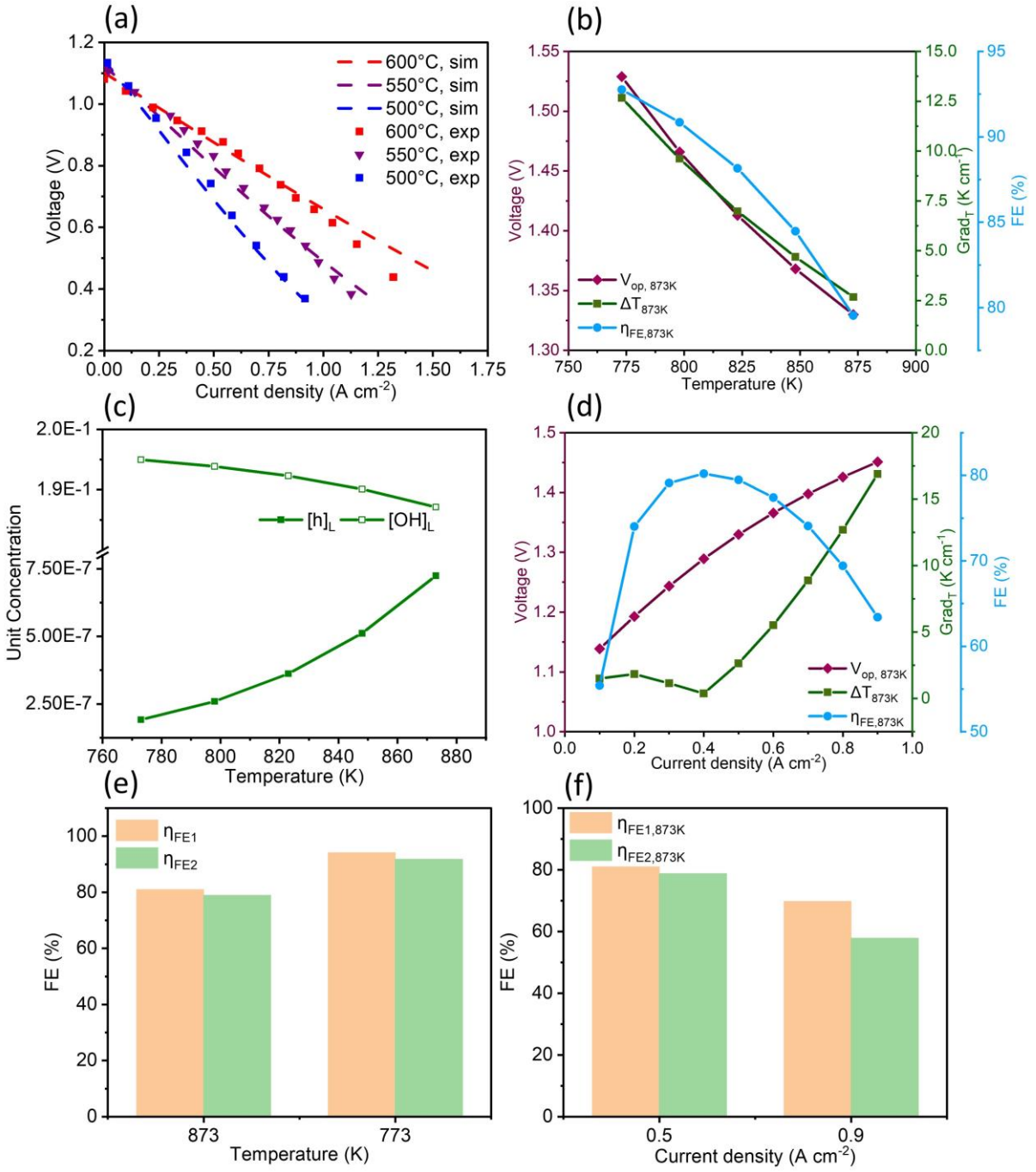

Figure 2 (a) Model validations; effects of working temperature on (b) the voltage, FE and temperature gradient, on (c) unit concentration of different charge carriers and on (e) upstream FE and downstream FE; effects of current density on (d) the voltage, FE and temperature gradient and on (f) upstream FE and downstream FE.

As illustrated in Figure 2 (b), with the increase of working temperature, both applied voltage and temperature gradient decreases monotonically. In this study, the current leakage phenomenon is indicated by the Faradaic efficiency (FE) value. FE is calculated by multiplying the hydrogen production rate by 2F (where F is the Faraday constant) and dividing this result by the applied current density. It is important to note that the numerator of this equation (2F times the hydrogen production rate) is equal to the imposed current density minus the current lost to leakage. As a result, when the current density is held constant, FE will increase as the leakage current decreases, and conversely, FE will decrease as the leakage current increases. The FE also shows the same trend as the change in working temperature. This can be explained by the results exhibited in Figure 2 (c), where $[h^{\cdot}]_L$ is nearly tripled and $[OH^{\cdot}]_L$ decreases by around 4% as the working temperature increases from 773 K to 873 K. $[h]_L$ represents the concentration of electronic hole in lattice unit. Electronic holes can react with electrons, which is why current leakage occurs. The molar flux of electronic hole is proportional to the $[h]_L$. Thus, the sensitivity of $[h]_L$ to working temperature (Figure 2 (c)) is equivalent to the sensitivity of leakage current to working temperature, which is in turn equivalent to the sensitivity of FE to working temperature. Additionally, as shown in Figure 2 (c), the $[h]_L$ increases with increasing working temperature, indicating that the leakage current increases as well. Therefore, the FE will decrease with increasing working temperature at 0.5 A cm^{-2}. Furthermore, upstream FE ($\eta_{FE,1}$) and downstream FE ($\eta_{FE,2}$) are presented in this work, to investigate the effects of various parameters on the FE distribution within the PCEC. As shown in Figure 2 (e), as the operating temperature increases, the difference between upstream FE and downstream FE becomes negligible.

In Figure 2 (d), as expected, the applied voltage increases gradually with the increase of current density. While the FE increases sharply with the initial increase of current density, which is consistent with the previously reported data in Ref. [12]. The peak FE of 82% is obtained at a

current density of 0.4 A cm^{-2}. However, the FE of PCEC decreases with increasing current density and is approximately 62.5% when the current density is 0.9 A cm^{-2}. This observation of the present model is contrary to the data reported in Ref. [12] because the heat transfer within the PCEC is accounted for in this work. Noteworthy, in this work, the temperature gradient within the cell is defined as the maximum temperature minus the minimum temperature, then divided by the length of the whole cell. Hence, the temperature gradient is consistently positive. Before reaching the thermal-neutral voltage (TNV), the heat adsorbed by steam electrolysis reaction is greater than the ohmic heat and the polarization heat. Therefore, the PCEC is in endothermic mode when the voltage is < TNV. At 0 A cm^{-2}, the temperature gradient should be zero (no heat generated or adsorbed). At 0.1 A cm^{-2}, the temperature gradient increases to 1.4 K cm^{-1} (endothermic). At 0.4 A cm^{-2}, the temperature gradient decreases to 0 K cm^{-1} (thermal-neutral). Hence, as the current density increases, the temperature gradient initially increases then decreases before reaching the TNV. Additionally, with a further increase in the current density, the generated ohmic heat and polarization heat surpass the electrolytic adsorbed heat, making PCEC in the exothermic operation mode. To better evaluate the performance of the PCEC with regards to hydrogen production, the upstream FE and the downstream FE are introduced. The upstream FE measures the FE of the first half section of the PCEC, and the downstream FE measures the other. By comparing the upstream and downstream FE, valuable insights can be gained into the performance differences between two sections of the PCEC. If there is a significant difference between the upstream and downstream FE, it may suggest that certain parts of the cell are not performing optimally, leading to inefficiencies. Therefore, it is essential to compare the upstream and downstream FE. In Figure 2 (e), when the current density is 0.4 A cm^{-2}, the difference between the upstream FE and downstream FE is around 13.9%. However, when the current density is 0.9 A cm^{-2}, the difference between the upstream FE and downstream FE considerably increases to 26.5%. This

indicates that increasing the current density can remarkably widen the gap between the upstream FE and the downstream FE, causing the energy efficiency downstream of the PCEC less than expected.

4.1.2 Effects of inlet flow rate

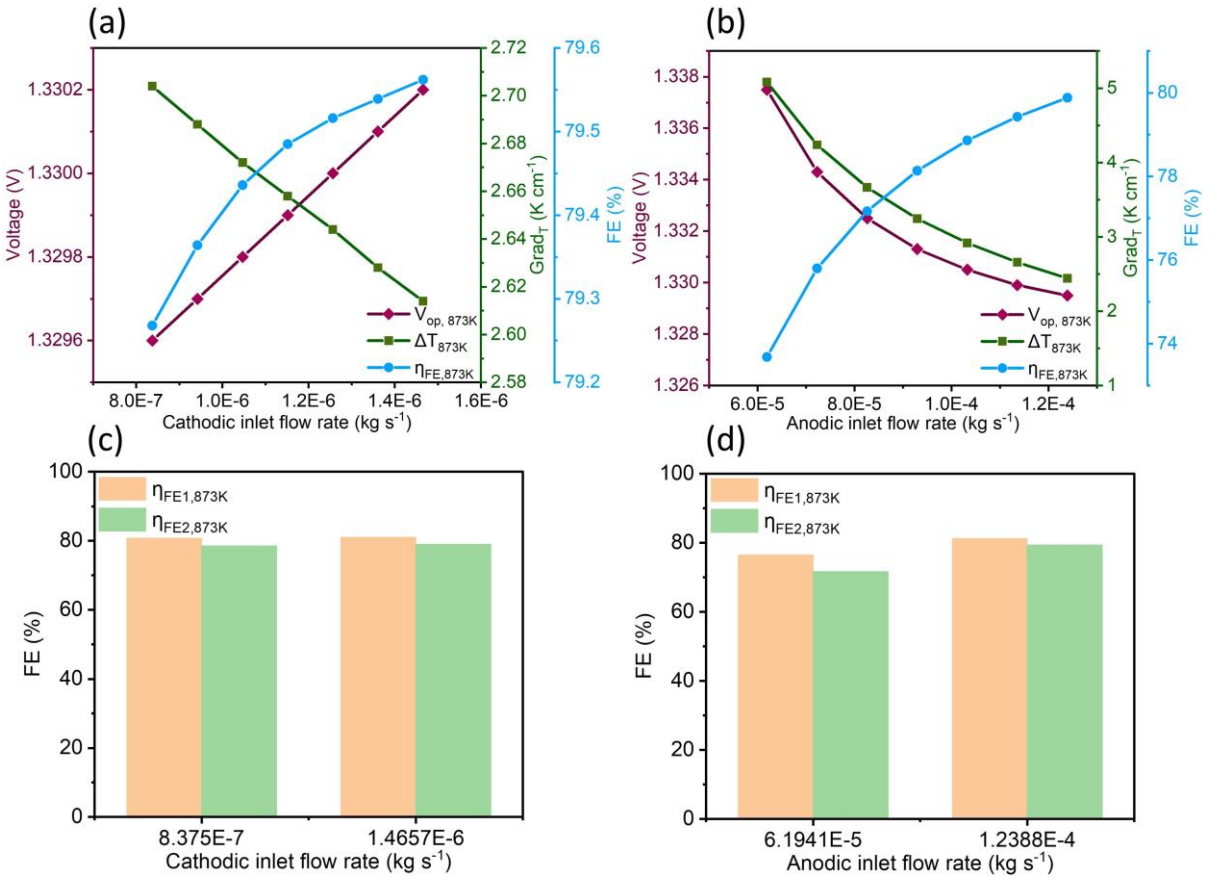

Figure 3 Effects of cathodic inlet flow rate on (a) the voltage, FE and temperature gradient and on (c) upstream FE and downstream FE; effects of anodic inlet flow rate on (b) the voltage, FE and temperature gradient and on (d) upstream FE and downstream FE.

Since either an increase in the anodic inlet flow rate or in the cathodic inlet flow rate can remove the heat from the PCEC, the temperature gradient decreases monotonically as expected (Figure 3 (a) and (b)). Correspondingly, the FE of PCEC is improved with increasing inlet flow rate either in the anode or in the cathode. Although the applied voltage increases with the increase of cathodic inlet flow rate, the increase is negligible (< 0.04%) (Figure 3 (a)). As the anodic inlet flow rate increases, the concentration of reactants within the electrode can be maintained at a higher level, which can reduce the concentration polarization effect and lead to a decrease

in applied voltage. However, its effect on the applied voltage is negligible. When the anode inlet flow is doubled, the applied voltage only increases by about 0.6%. In Figure 3 (d), FE distribution becomes more uniform due to the increased anodic inlet flow. This can be attributed to two consequences of increased flow: 1) more uniform distribution of reactants 2) more uniform temperature distribution (decreased temperature gradient). Therefore, the environment of upstream and downstream of PCEC becomes more similar, leading to a more uniform FE distribution.

4.1.3 Effects of inlet steam molar fraction

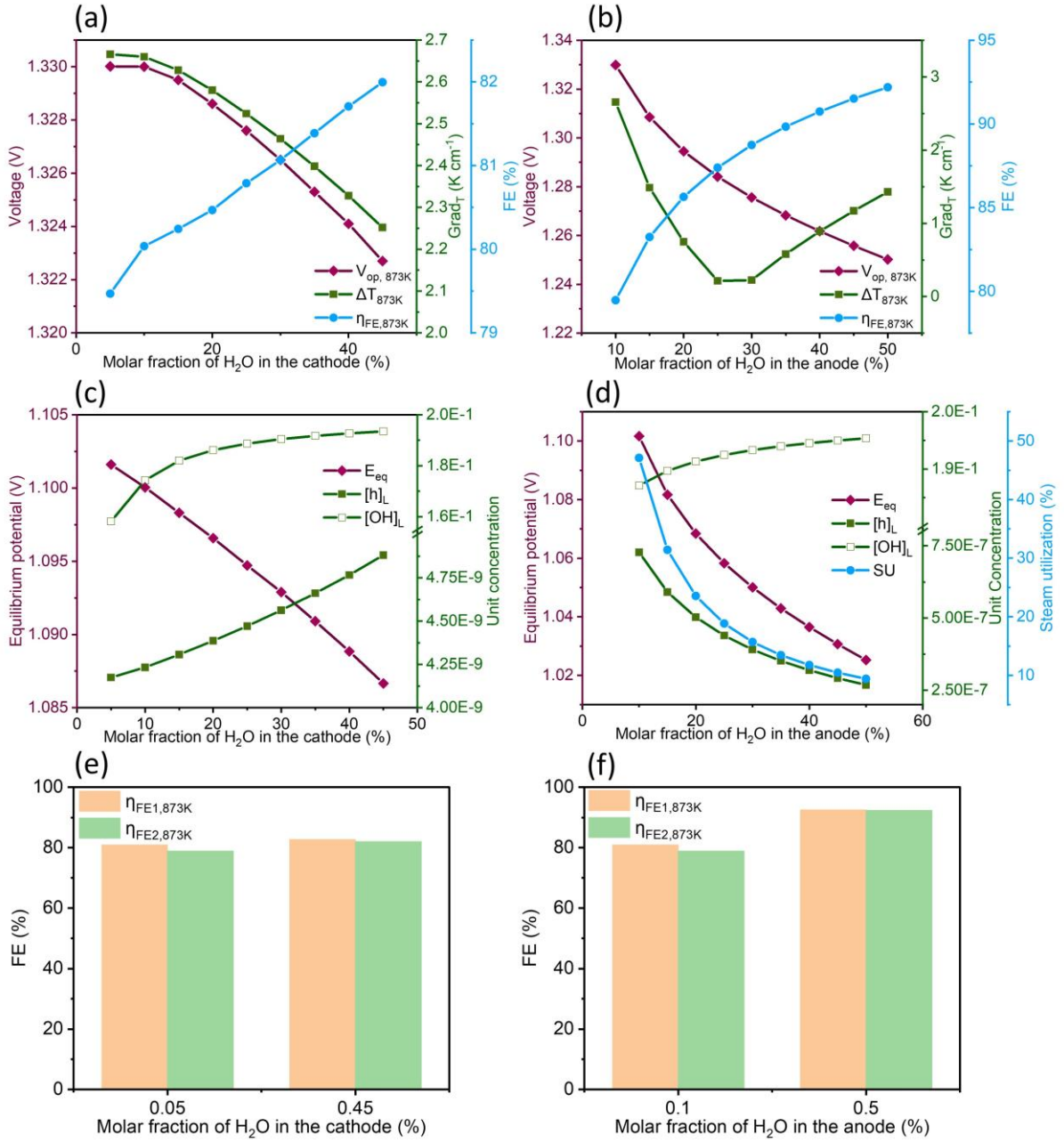

Figure 4 Effects of cathodic inlet steam molar fraction on (a) the voltage, FE and temperature gradient, on (c) the equilibrium potential and unit concentration of different charge carriers and on (e) upstream FE and downstream FE; effects of anodic inlet steam molar fraction on (b) the voltage, FE and temperature gradient, on (d) the equilibrium potential, the unit concentration of different charge carriers and steam utilization and on (f) upstream FE and downstream FE.

With an increase in the cathodic inlet steam molar fraction, the applied voltage decreases continuously (Figure 4 (a)). The increased cathodic inlet steam molar fraction leads to a reduction in the partial pressure of H_2, leading to a decrease in the equilibrium potential of PCEC (Figure 4 (c)). It is also found that the temperature gradient decreases slightly as the

cathodic inlet steam molar fraction increases. Furthermore, the enhanced moist environment in the cathode substantially promotes the formation of proton defects even if the formation of holes is slightly improved as well. Consequently, the FE increases with increasing cathodic inlet steam molar fraction. Besides, the applied voltage also decreases with the increase of the anodic inlet steam molar fraction (Figure 4 (b)). The increased anodic inlet steam molar fraction can increase the partial pressure of H_2O within the PCEC, resulting in a decrease in the equilibrium potential (Figure 4 (d)). It can also be observed from Figure 4 (b) that, when the anodic inlet steam molar fraction increases to 20%, the applied voltage approaches TNV, thereby making the temperature gradient in the cell equal to zero. Subsequently, with a further increase in anodic steam molar fraction, the applied voltage becomes smaller than TNV, making endothermic operation of PCEC. Furthermore, the increased anodic inlet steam molar fraction can strongly suppress the formation of holes since the partial pressure of oxygen in the anode is reduced (Figure 4 (d)). Considering both temperature and defects concentration effects, the FE can be enhanced by increasing the anodic steam molar fraction. Impressively, in Figure 4 (e) and (f), the difference between the upstream FE and the downstream FE approaches zero by increasing the inlet steam molar fraction either in the anode or in the cathode. From this point of view, increasing the inlet steam molar fraction is beneficial to the uniform distribution of FE. Nevertheless, it is worth noting that although increasing the anodic inlet steam molar fraction is an effective way to reduce the temperature gradient and improve FE, the steam utilization is remarkably reduced (Figure 4 (d)). This is detrimental to the overall energy efficiency of PCEC. Moreover, if the anodic inlet steam molar fraction is increased, it will result in the dilution of produced hydrogen. This means that a separation process must be implemented to obtain pure hydrogen, and this additional step can decrease the overall efficiency of the system and increase its cost. Therefore, it is crucial to exercise careful control over the cathodic inlet steam fraction from the perspective of the entire PCEC system.

4.2 DOE

4.2.1 Applied voltage as the response

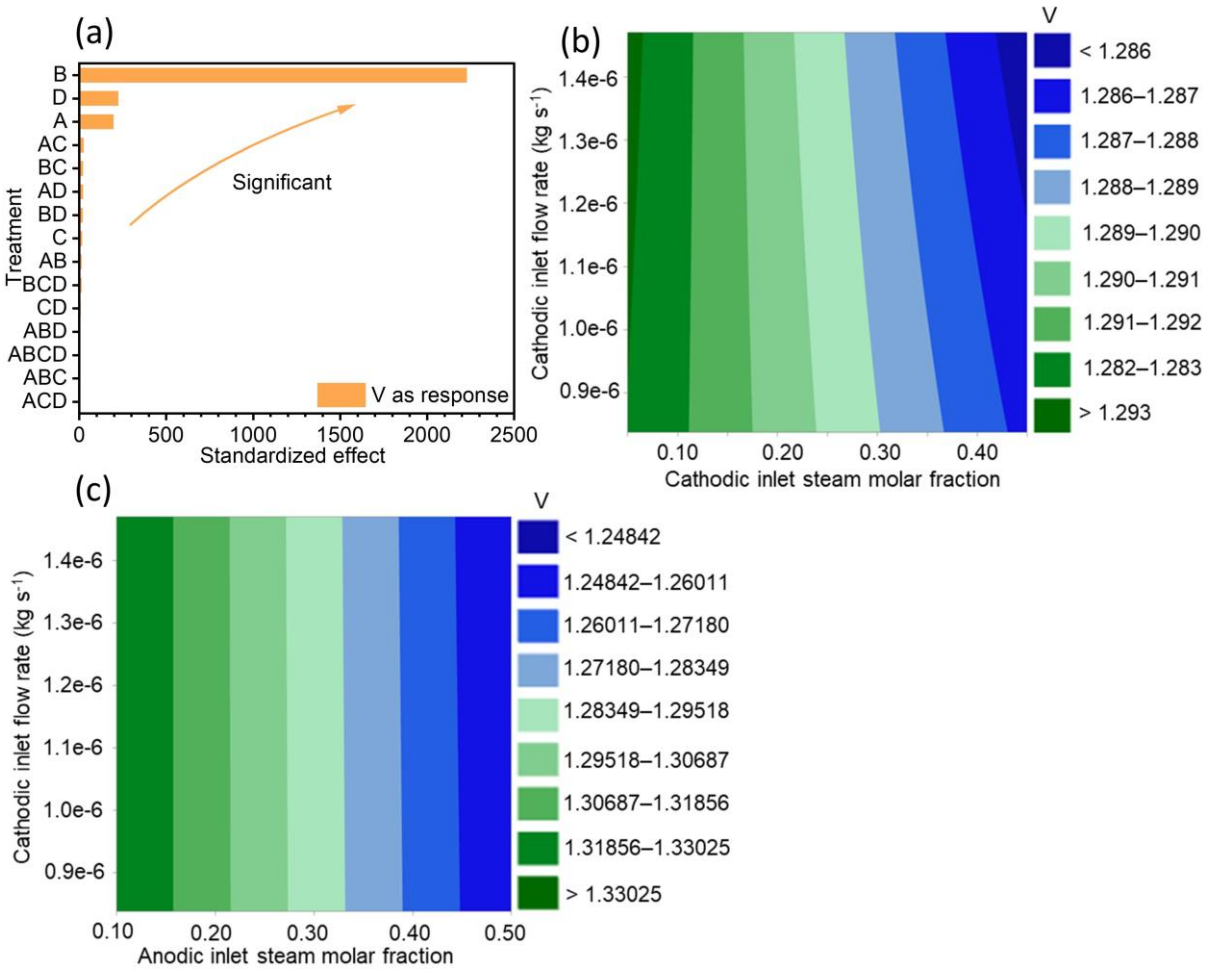

Figure 5 When the applied voltage is the response: (a) standardized effects of different parameters' treatments, contour maps of interactions between (b) cathodic inlet flow rate and cathodic inlet steam molar fraction, between (c) cathodic inlet flow rate and anodic inlet steam molar fraction.

Figure 5 (a) shows the order of different parameters based on their importance. The most important factor to the applied voltage is the anodic inlet steam molar fraction. Additionally, the top five important treatments are: B > D > A > AC > BC. Figure 5 (b) and (c) demonstrate the contour map of AC and BC interaction effects, respectively. In Figure 5 (b), it can be found that, compared to the main effect of cathodic inlet steam molar fraction, the main effect of cathodic inlet flow rate is negligible. Furthermore, the interaction of AC on the applied voltage tends to increase the voltage when the cathodic inlet steam molar fraction is < 0.18, whereas

the opposite effect is observed when the cathodic inlet steam molar fraction is > 0.18. This opposite effect becomes more remarkable as the cathodic inlet steam molar fraction increases. In Figure 5 (c), the interaction of BC is considerably weaker than that of AC.

The effect of a factor on a response variable is divided into two types: 1) If the response variable increases with the increase of the factor, its effect is positive; 2) If the response variable decreases with the increase of the factor, its effect is negative. Therefore, according to the impact types of different factors, it is possible to qualitatively understand how different factors affect the performance of PCEC. Moreover, under the practical PCEC operation, when the current density is fixed, reducing the applied voltage can be one of the optimization goals for saving the electric power. Therefore, understanding the negative impact of different parameters on the applied voltage is also important for planning PCEC operational strategies. As listed in Table 5, the anodic inlet steam molar fraction exhibits the most negative effect on the applied voltage. In other words, when reducing the applied voltage is the goal, then increasing the anodic inlet steam molar fraction can be the most effective tactic. The standardized effect of anodic inlet flow rate and cathodic inlet steam molar fraction is significantly less than that of anodic inlet steam molar fraction. Additionally, although the negative of anodic inlet flow rate is not as important as inlet steam molar fraction, the interaction effects of AC and BC cannot be ignored.

Table 5 Order of different treatments.

Cases	**Order of different treatments**
Negative impacts on the applied voltage	B > D > A > AC > BC > AD > C > AB > CD
Negative impacts on the temperature gradient	B > D > C > ABD > BCD > A > ABCD > AC
Positive impacts on the FE	B > D > A > BCD > C > ABD > ABC

4.2.2 Temperature gradient as the response

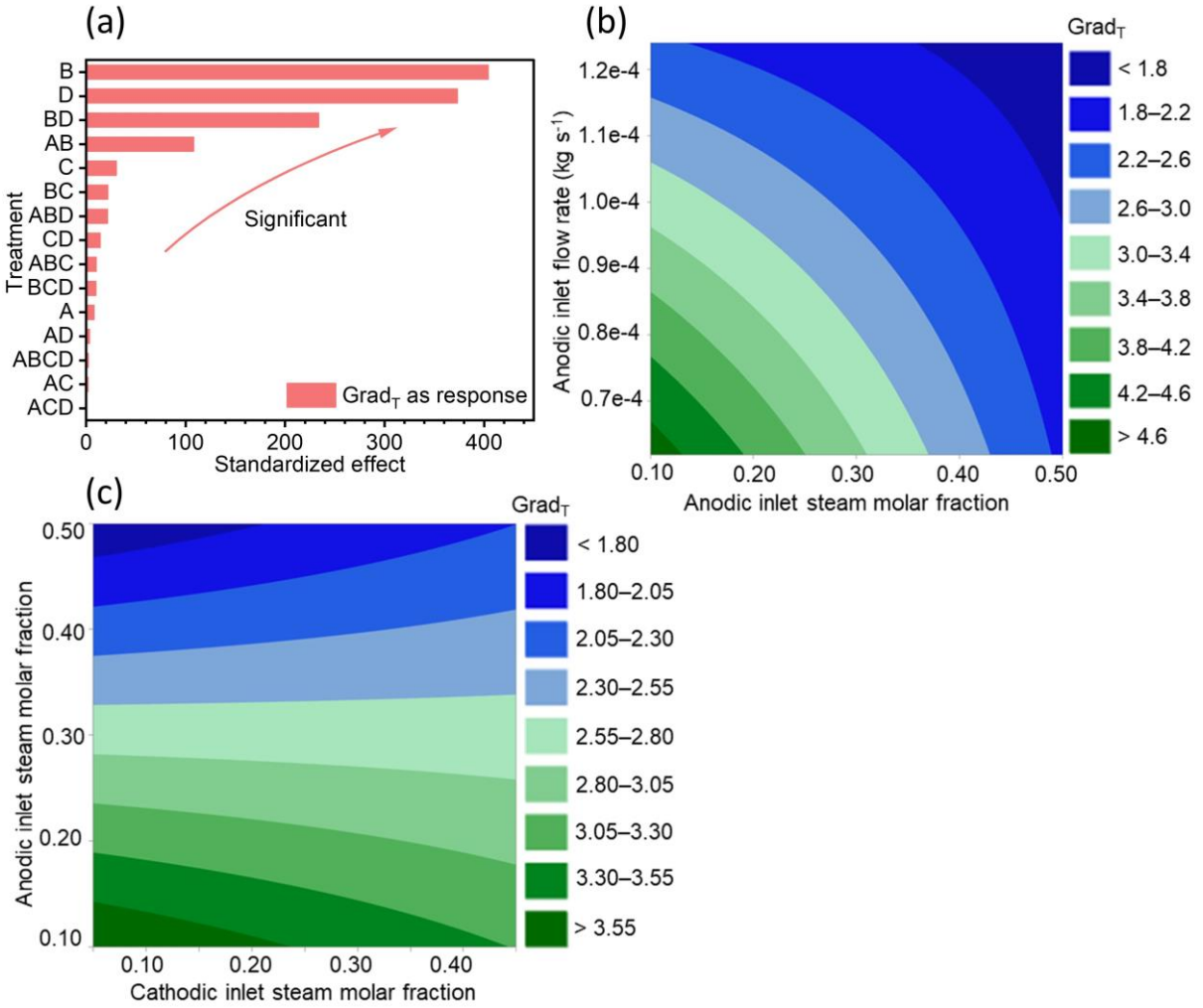

Figure 6 When the temperature gradient is the response: (a) standardized effects of different parameters' treatments, contour maps of interactions between (b) anodic inlet flow rate and anodic inlet steam molar fraction, between (c) anodic steam molar fraction and cathodic inlet steam molar fraction.

As illustrated in Figure 6 (a), the anodic inlet steam molar fraction is still the most significant factor, when the temperature gradient is the response. The top five important treatments are: B > D > BD > AB > C. In Figure 6 (b), it can also demonstrate that the main effects of anodic inlet flow rate and anodic inlet steam molar fraction are comparable. While the interaction of BD is more substantial with increasing anodic inlet steam molar fraction. In Figure 6 (c), the

main effect of the anodic inlet steam molar fraction is more significant than that of the cathodic inlet steam molar fraction. When the anodic inlet steam molar fraction is < 0.3, the interaction of AB on the temperature gradient tends to reduce the temperature gradient. However, the opposite interaction effect is observed when the anodic inlet steam molar fraction is > 0.3. Furthermore, to sustain the robust performance of the PCEC and promote the life span, reducing the temperature gradient can be an optimization target [38]. Table 5 shows that the anodic inlet steam molar fraction exhibits the most negative effect on the temperature gradient. Additionally, the second effective parameter is the anodic inlet steam molar fraction.

4.2.3 Faraday efficiency as the response

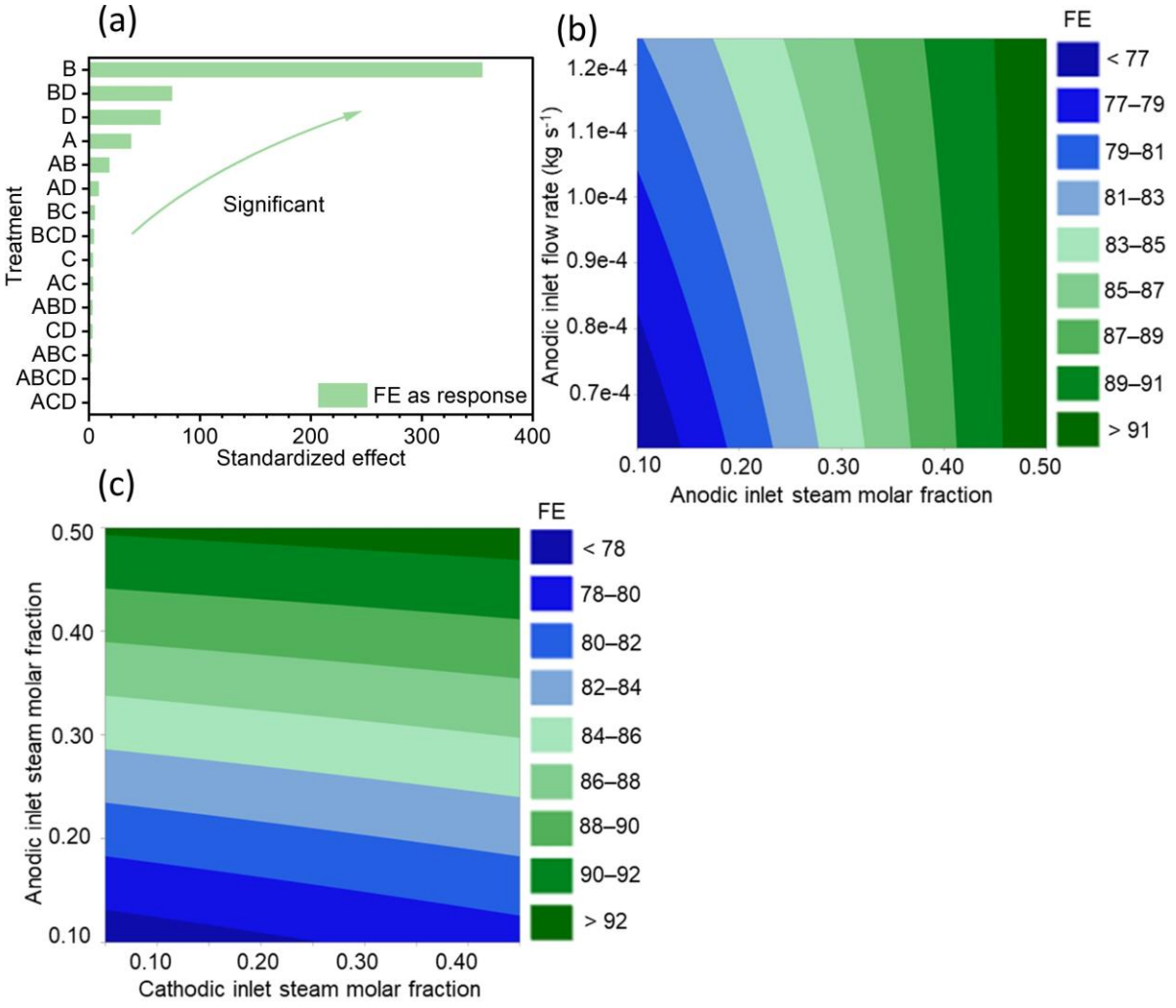

Figure 7 When FE is the response: (a) standardized effects of different parameters' treatments, contour maps of interactions between (b) anodic inlet flow rate and cathodic inlet steam molar fraction, between (c) anodic inlet steam molar fraction and cathodic inlet steam molar fraction.

Figure 7 (a) shows that, when the FE is the response, the most important factor is still the anodic inlet steam molar fraction. The top five important treatments are: B > BD > D > A > AB. It is worth noting that the standardized effects of the anodic inlet steam molar fraction are more than four times of that of the second important treatment (interaction of BD). Consequently, it indicates that the effect of the anodic inlet steam molar fraction on the FE is dominant. It can be found in Figure 7 (b) that, the interaction of BD is more significant under a low anodic inlet steam molar fraction than that under a high anodic inlet steam molar fraction. In Figure 7 (c), the interaction of AB is evidently weaker than that of BD. To enhance the energy efficiency of PCEC, the FE can also be an optimization goal. The treatments with a positive effect on the FE are summarized in Table 5. The anodic inlet steam molar fraction possesses the most important impact on maximizing the FE of PCEC. Furthermore, the second effective parameter is the anodic inlet steam molar fraction.

4.2.4 Regression model

To this point, the DOE results for different responses are analysed separately. According to the above discussion, the anodic inlet steam fraction and anodic inlet flow rate are two of the most significant factors. For the operation of PCEC, adjusting the anodic inlet steam fraction and anodic inlet flow rate are the most efficient strategies to regulate the applied voltage, temperature gradient and faraday efficiency. In other words, adjusting the anode operating parameters is more beneficial and more effective in controlling the performance of PCEC than adjusting the cathode operating parameters. Therefore, to optimize the performance of PCEC, more efforts should be made in the future to further optimize the anode inlet steam fraction and anode inlet flow rate. Besides, for each response, a regression model can be derived by applying DOE. Table 6 lists the three regression models obtained from DOE analysis, in which the terms of insignificant treatment are excluded. Three responses of PCEC under different conditions are calculated by using both the 2D Multiphysics model and regression models. In addition, to

verify the effectiveness of different regression models, the coefficient of determination (R^2) is calculated for each response, which is listed in Table 6 as well. The value of R^2 is acceptable. In this light, the regression model attained from DOE show a potential capability to be used as a surrogate model for the 2D numerical model. It reveals the power of the DOE method, which can be widely used in the future theoretical research of PCEC.

Table 6 The regression models.

Response	**Regression model**	**R^2**
V	$1.36 - 5.73 \times 10^{-3} \cdot xc\_in - 0.19 \cdot xa\_in + 5.52 \times 10^{3} \cdot vc\_in - 92.73 \cdot va\_in + 8.7 \times 10^{-4} \cdot xc\_in \cdot xa\_in - 4.22 \times 10^{3} \cdot xc\_in \cdot vc\_in - 34.7 \cdot xc\_in \cdot va\_in - 1.29 \times 10^{4} \cdot xa\_in \cdot vc\_in - 46.9 \cdot xa\_in \cdot va\_in - 3.27 \times 10^{7} \cdot vc\_in \cdot va\_in + 8.06 \times 10^{7} \cdot xa\_in \cdot vc\_in \cdot va\_in$	0.97
$Grad_T$	$10.11 - 1.83 \cdot xc\_in - 15.03 \cdot xa\_in - 7.63 \times 10^{5} \cdot vc\_in - 5.80 \times 10^{4} \cdot va\_in + 5.84 \cdot xc\_in \cdot xa\_in - 9.434 \times 10^{5} \cdot xc\_in \cdot vc\_in + 7.62 \times 10^{3} \cdot xc\_in \cdot va\_in + 1.02 \times 10^{6} \cdot x\_h2oa \cdot vc\_in + 9.70 \times 10^{4} \cdot xa\_in \cdot va\_in + 5.25 \times 10^{9} \cdot vc\_in \cdot va\_in + 2.80 \times 10^{6} \cdot xc\_in \cdot xa\_in \cdot vc\_in - 2.29 \times 10^{4} \cdot xc\_in \cdot xa\_in \cdot va\_in - 7.73 \times 10^{9} \cdot xa\_in \cdot vc\_in \cdot va\_in - 1.17 \times 10^{10} \cdot xc\_in \cdot xa\_in \cdot vc\_in \cdot va\_in$	0.93
FE	$57.45 + 12.11 \cdot xc\_in + 69.92 \cdot xa\_in + 2.79 \times 10^{6} \cdot vc\_in + 1.48 \times 10^{5} \cdot va\_in - 13.10 \cdot xc\_in \cdot xa\_in - 1.33 \times 10^{6} \cdot xc\_in \cdot vc\_in - 3.16 \times 10^{4} \cdot xc\_in \cdot va\_in - 5.67 \times 10^{6} \cdot xa\_in \cdot vc\_in - 3.00 \times 10^{5} \cdot xa\_in \cdot va\_in - 1.69 \times 10^{10} \cdot vc\_in \cdot va\_in - 3.22 \times 10^{5} \cdot xc\_in \cdot xa\_in \cdot vc\_in - 3.27 \times 10^{3} \cdot xc\_in \cdot xa\_in \cdot va\_in + 3.45 \times 10^{10} \cdot xa\_in \cdot vc\_in \cdot va\_in$	0.94

5. Conclusions

In this study, a 2D model is developed for a PCEC to investigate the effects of different parameters on the applied voltage, faraday efficiency and temperature gradients. The heat transport within the PCEC is considered, allowing a more realistic description of the current leakage phenomenon. Furthermore, a framework combining 2D numerical model, OFAT

method and DOE method is constructed to reveal the main and interaction effects of different operating parameters.

By using OFAT method, the peak FE of 82% is obtained at 600 °C and a current density of 0.4 A cm^{-2}. A further increase of current density decreases the FE. The non-uniformity of FE distribution increases with increasing current density. The temperature gradient of the cell decreases with the increase of inlet flow rate, while the FE shows the opposite trend. The applied voltage and temperature gradient decrease with increasing inlet steam molar fraction, while FE increases continuously. In addition, by analysing DOE results, the anodic inlet steam molar fraction and the anodic inlet flow rate are found to be the most significant factors. When the applied voltage is the response, the interaction between the cathodic inlet steam molar fraction and the cathodic inlet flow rate is important. The interaction between the anodic inlet steam molar fraction and the anodic inlet flow rate are found to be significant when the temperature gradient or the FE is the response. Moreover, three regression models are derived from the DOE results. The good validity of the regression model shows its potential ability as a surrogate model for 2D numerical model. In summary, the main contribution of this study is the development a framework to combine the numerical model with OFAT method and DOE method. Such a framework can provide deep insights in the effects and interactions of different parameters. Moreover, the significant parameters and interactions can be identified, thereby enhancing the understanding of PCEC.

Acknowledgments

M. NI thanks the grant (Project Number: N_PolyU552/20) from Research Grants Council, University Grants Committee, Hong Kong SAR.

References

[1] R.-H. Lin, Y.-Y. Zhao, and B.-D. Wu, 'Toward a hydrogen society: Hydrogen and smart grid integration', *Int. J. Hydrog. Energy*, vol. 45, no. 39, pp. 20164–20175, Aug. 2020, doi: 10.1016/j.ijhydene.2020.01.047.

[2] P. Nikolaidis and A. Poullikkas, 'A comparative overview of hydrogen production processes', *Renew. Sustain. Energy Rev.*, vol. 67, pp. 597–611, Jan. 2017, doi: 10.1016/j.rser.2016.09.044.

[3] Hydrogen and Fuel Cell Technologies Office, 'Hydrogen Production: Natural Gas Reforming', *Energy.gov*. https://www.energy.gov/eere/fuelcells/hydrogen-production-natural-gas-reforming.

[4] M. Yu, K. Wang, and H. Vredenburg, 'Insights into low-carbon hydrogen production methods: Green, blue and aqua hydrogen', *Int. J. Hydrog. Energy*, vol. 46, no. 41, pp. 21261–21273, Jun. 2021, doi: 10.1016/j.ijhydene.2021.04.016.

[5] B. Chen et al., "Syngas/power cogeneration from proton conducting solid oxide fuel cells assisted by dry methane reforming: A thermal-electrochemical modelling study," Energy Conversion and Management, vol. 167, pp. 37–44, Jul. 2018, doi: 10.1016/j.enconman.2018.04.078.

[6] H. Xu, B. Chen, H. Zhang, Q. Sun, G. Yang, and M. Ni, "Modeling of direct carbon solid oxide fuel cells with H2O and CO2 as gasification agents," International Journal of Hydrogen Energy, vol. 42, no. 23, pp. 15641–15651, Jun. 2017, doi: 10.1016/j.ijhydene.2017.05.075.

[7] M. Ni, M. K. H. Leung, and D. Y. C. Leung, 'Theoretical analysis of reversible solid oxide fuel cell based on proton-conducting electrolyte', *J. Power Sources*, vol. 177, no. 2, pp. 369–375, Mar. 2008, doi: 10.1016/j.jpowsour.2007.11.057.

[8] J. Guan, S. E. Dorris, U. Balachandran, and M. Liu, ‘Transport properties of BaCe0.95Y0.05O3−α mixed conductors for hydrogen separation’, *Solid State Ion.*, vol. 100, no. 1, pp. 45–52, Sep. 1997, doi: 10.1016/S0167-2738(97)00320-2.

[9] S. Choi, T. C. Davenport, and S. M. Haile, ‘Protonic ceramic electrochemical cells for hydrogen production and electricity generation: exceptional reversibility, stability, and demonstrated faradaic efficiency’, *Energy Environ. Sci.*, vol. 12, no. 1, pp. 206–215, 2019, doi: 10.1039/C8EE02865F.

[10] J.-H. Zhang, L.-B. Lei, D. Liu, F.-Y. Zhao, M. Ni, and F. Chen, ‘Mathematical modeling of a proton-conducting solid oxide fuel cell with current leakage’, *J. Power Sources*, vol. 400, pp. 333–340, Oct. 2018, doi: 10.1016/j.jpowsour.2018.08.038.

[11] R. J. Kee, H. Zhu, B. W. Hildenbrand, E. Vøllestad, M. D. Sanders, and R. P. O’Hayre, ‘Modeling the Steady-State and Transient Response of Polarized and Non-Polarized Proton-Conducting Doped-Perovskite Membranes’, *J. Electrochem. Soc.*, vol. 160, no. 3, p. F290, Jan. 2013, doi: 10.1149/2.016304jes.

[12] H. Zhu and R. J. Kee, ‘Membrane polarization in mixed-conducting ceramic fuel cells and electrolyzers’, *Int. J. Hydrog. Energy*, vol. 41, no. 4, pp. 2931–2943, Jan. 2016, doi: 10.1016/j.ijhydene.2015.10.100.

[13] D. D. Frey, F. Engelhardt, and E. M. Greitzer, ‘A role for “one-factor-at-a-time” experimentation in parameter design’, *Res. Eng. Des.*, vol. 14, no. 2, pp. 65–74, May 2003, doi: 10.1007/s00163-002-0026-9.

[14] J. Antony, *Design of experiments for engineers and scientists*, 2nd edition. in Elsevier insights. London: Elsevier, 2014.

[15] Z. Li *et al.*, 'Direct ammonia protonic ceramic fuel cell: A modelling study based on elementary reaction kinetics', *J. Power Sources*, vol. 556, p. 232505, Feb. 2023, doi: 10.1016/j.jpowsour.2022.232505.

[16] Y. Luo *et al.*, 'Coupling ammonia catalytic decomposition and electrochemical oxidation for solid oxide fuel cells: A model based on elementary reaction kinetics', *J. Power Sources*, vol. 423, pp. 125–136, May 2019, doi: 10.1016/j.jpowsour.2019.03.064.

[17] P. Costamagna, P. Costa, and V. Antonucci, 'Micro-modelling of solid oxide fuel cell electrodes', *Electrochim. Acta*, vol. 43, no. 3–4, pp. 375–394, Jan. 1998, doi: 10.1016/S0013-4686(97)00063-7.

[18] M. Suzuki and T. Oshima, 'Estimation of the Co-ordination number in a Multi-Component Mixture of Spheres', *Powder Technol.*, vol. 35, no. 2, pp. 159–166, Jul. 1983, doi: 10.1016/0032-5910(83)87004-1.

[19] K. Li, T. Araki, T. Kawamura, A. Ota, and Y. Okuyama, 'Numerical analysis of current efficiency distributions in a protonic ceramic fuel cell using Nernst-Planck-Poisson model', *Int. J. Hydrog. Energy*, vol. 45, no. 58, pp. 34139–34149, Nov. 2020, doi: 10.1016/j.ijhydene.2020.09.143.

[20] C. Peters, *Grain-size Effects in Nanoscaled Electrolyte and Cathode Thin Films for Solid Oxide Fuel Cells (SOFC)*. KIT Scientific Publishing, 2009.

[21] C. Duan *et al.*, 'Highly efficient reversible protonic ceramic electrochemical cells for power generation and fuel production', *Nat. Energy*, vol. 4, no. 3, pp. 230–240, Mar. 2019, doi: 10.1038/s41560-019-0333-2.

[22] H. Zhu, S. Ricote, C. Duan, R. P. O'Hayre, D. S. Tsvetkov, and R. J. Kee, 'Defect Incorporation and Transport within Dense $BaZr_{0.8}Y_{0.2}O_{3-\delta}$ (BZY20) Proton-Conducting

Membranes', *J. Electrochem. Soc.*, vol. 165, no. 9, p. F581, May 2018, doi: 10.1149/2.0161809jes.

[23] M. Ni, M. K. H. Leung, and D. Y. C. Leung, 'Parametric study of solid oxide steam electrolyzer for hydrogen production', *Int. J. Hydrog. Energy*, vol. 32, no. 13, pp. 2305–2313, Sep. 2007, doi: 10.1016/j.ijhydene.2007.03.001.

[24] S. B. Beale *et al.*, 'Continuum scale modelling and complementary experimentation of solid oxide cells', *Prog. Energy Combust. Sci.*, vol. 85, p. 100902, Jul. 2021, doi: 10.1016/j.pecs.2020.100902.

[25] Z. Li *et al.*, 'Protonic ceramic fuel cells for power-ethylene cogeneration: A modelling study on structural parameters', *Energy*, vol. 264, p. 126193, Feb. 2023, doi: 10.1016/j.energy.2022.126193.

[26] Y. Jiang and A. V. Virkar, 'Fuel Composition and Diluent Effect on Gas Transport and Performance of Anode-Supported SOFCs', *J. Electrochem. Soc.*, vol. 150, no. 7, p. A942, May 2003, doi: 10.1149/1.1579480.

[27] R. S. Brokaw, 'Predicting Transport Properties of Dilute Gases', *Ind. Eng. Chem. Process Des. Dev.*, vol. 8, no. 2, pp. 240–253, Apr. 1969, doi: 10.1021/i260030a015.

[28] M. Błesznowski, M. Sikora, J. Kupecki, Ł. Makowski, and W. Orciuch, 'Mathematical approaches to modelling the mass transfer process in solid oxide fuel cell anode', *Energy*, vol. 239, p. 121878, Jan. 2022, doi: 10.1016/j.energy.2021.121878.

[29] Q. Xu, L. Xia, Q. He, Z. Guo, and M. Ni, 'Thermo-electrochemical modelling of high temperature methanol-fuelled solid oxide fuel cells', *Appl. Energy*, vol. 291, p. 116832, Jun. 2021, doi: 10.1016/j.apenergy.2021.116832.

[30] Z. Li *et al.*, 'Ethylene and power cogeneration from proton ceramic fuel cells (PCFC): A thermo-electrochemical modelling study', *J. Power Sources*, vol. 536, p. 231503, Jul. 2022, doi: 10.1016/j.jpowsour.2022.231503.

[31] M. Ni, '2D thermal modeling of a solid oxide electrolyzer cell (SOEC) for syngas production by H2O/CO2 co-electrolysis', *Int. J. Hydrog. Energy*, vol. 37, no. 8, pp. 6389–6399, Apr. 2012, doi: 10.1016/j.ijhydene.2012.01.072.

[32] Z. Li *et al.*, 'Effects of cathode thickness and microstructural properties on the performance of protonic ceramic fuel cell (PCFC): A 3D modelling study', *Int. J. Hydrog. Energy*, vol. 47, no. 6, pp. 4047–4061, Jan. 2022, doi: 10.1016/j.ijhydene.2021.11.022.

[33] A. Freddi and M. Salmon, *Design Principles and Methodologies: From Conceptualization to First Prototyping with Examples and Case Studies*. in Springer Tracts in Mechanical Engineering. Cham: Springer International Publishing, 2019. doi: 10.1007/978-3-319-95342-7.

[34] J. Antony, Design of experiments for engineers and scientists, 2nd edition. in Elsevier insights. London: Elsevier, 2014.

[35] D. C. Montgomery, Design and analysis of experiments, Tenth edition. Hoboken, NJ: Wiley, 2020.

[36] M. F. Niri et al., "Quantifying key factors for optimised manufacturing of Li-ion battery anode and cathode via artificial intelligence," Energy and AI, vol. 7, p. 100129, Jan. 2022, doi: 10.1016/j.egyai.2021.100129.

[37] J. Wang et al., "Integration of multi-physics and machine learning-based surrogate modelling approaches for multi-objective optimization of deformed GDL of PEM fuel cells," Energy and AI, vol. 14, p. 100261, Oct. 2023, doi: 10.1016/j.egyai.2023.100261.

[38] Z. Zeng, Y. Qian, Y. Zhang, C. Hao, D. Dan, and W. Zhuge, ‘A review of heat transfer and thermal management methods for temperature gradient reduction in solid oxide fuel cell (SOFC) stacks’, *Appl. Energy*, vol. 280, p. 115899, Dec. 2020, doi: 10.1016/j.apenergy.2020.115899.